Chemical Engineering Journal

High-performance post-treatment-free PEDOT based thermoelectric with the establishment of long-range ordered conductive paths

--Manuscript Draft--

Manuscript Number:	
Article Type:	Research Paper
Section/Category:	Novel Materials for Energy and Advanced Applications
Keywords:	PEDOT:PSS; ionic liquid; thermoelectric; post-treatment-free; structure-property correlation
Corresponding Author:	Peng Zhang Sun Yat-Sen University Guangzhou, Guangdong CHINA
First Author:	Xin Li
Order of Authors:	Xin Li
	Zhenhang He
	Zhen Liu
	Yu Chen
	Zekun Zhou
	Guixiang Chen
	Weiheng Qi
	Daniel Rauber
	Christopher W. M. Kay
	Peng Zhang
Abstract:	In this work, post-treatment-free polymer hybrids, consisting of poly(3,4-ethylenedioxythiophene):poly(styrene sulfonate) (PEDOT:PSS) and ionic liquids (ILs), were fabricated for the thermoelectric (TE) application. By optimizing the ILs' molar concentration (0-0.5 M) and chemical composition, that is varying the cyano-based anions coupled with 1-ethyl-3-methylimidazolium cations, a superior TE performance (power factor of 190 μW m −1 K −2) was achieved. The excellent TE performance was attributed to the conductive network under the coupling effect of molecular structure (such as oxidation level, conformation and crystallization of PEDOT chains) and microstructure (long-range ordered conductive paths). Especially, the long-range conductive paths were proved to be made of rod-like microdomains, based on detailed structure analysis with micro-Fourier transform infrared spectroscopy and small-angle X-ray scattering. These paths enabled carrier transport among microdomains of PEDOT:PSS/IL hybrids. Moreover, the conductive network of PEDOT:PSS/IL hybrids showed good environmental and mechanical stability, enabling the fabrication of flexible TE generators.

Graphical Abstract

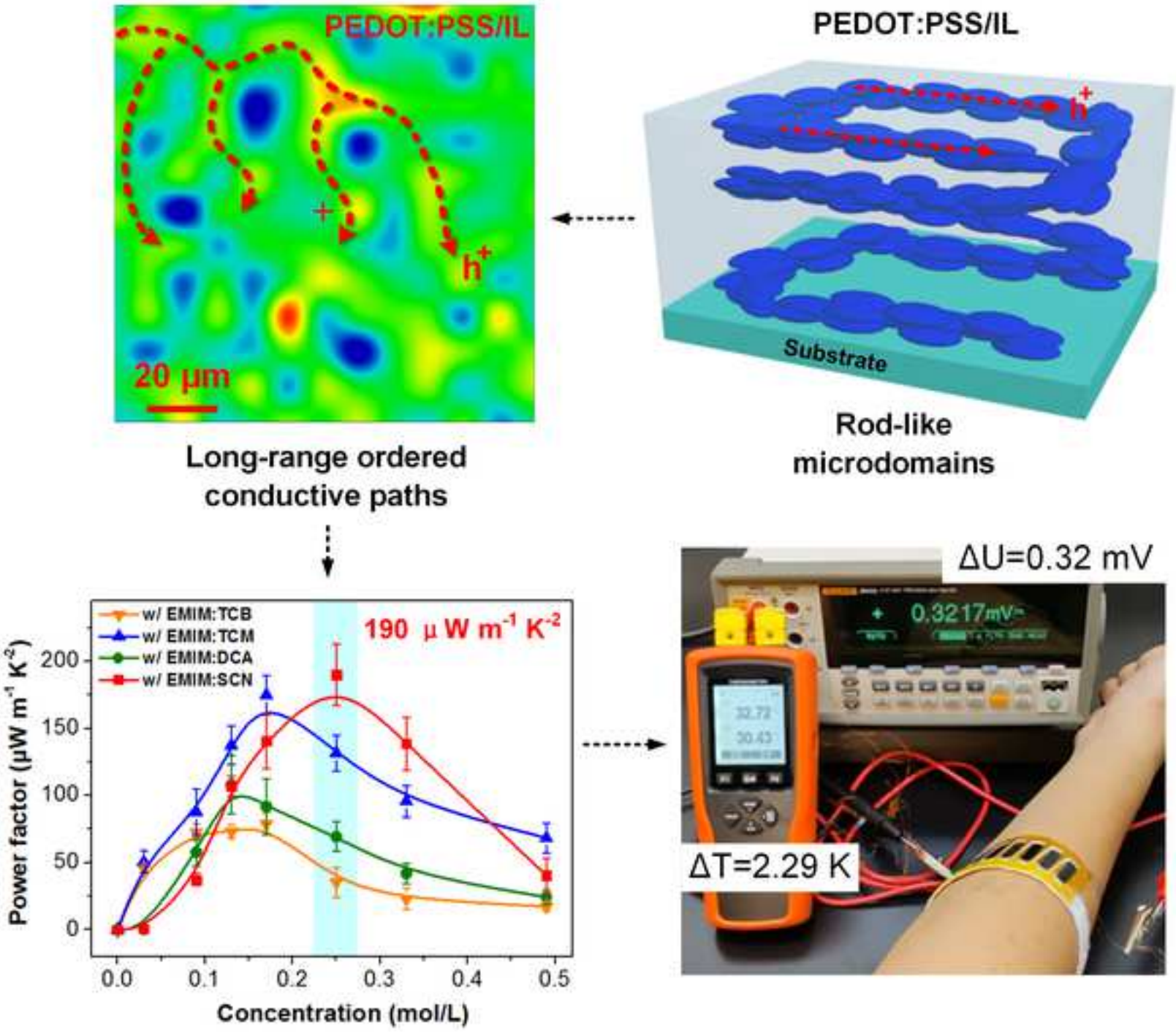

Highlights

1. Achieving a superior power factor value of 190 μW $m^{-1} K^{-2}$, the highest value ever reported in the post-treatment-free PEDOT-based thermoelectric.

2. The superior TE performance was attributed to the conductive network with balanced microstructure and molecular structure.

3. Evidencing the conductive network with long-range ordered conductive paths (LOCP) consisting of packed rod-like microdomains.

4. The LOCP enabled PEDOT:PSS/IL hybrids good environmental and mechanical stability, promising for the high perforamnce TEG applications.

High-performance post-treatment-free PEDOT based thermoelectric with the establishment of long-range ordered conductive paths

Xin Li,[a] Zhenhang He,[a] Zhen Liu,[a,*] Yu Chen,[b] Zekun Zhou,[a] Guixiang Chen,[a] Weiheng Qi,[b,c] Daniel Rauber,[d] Christopher W. M. Kay,[d] Peng Zhang[a,*]

[a] *School of Materials Science and Engineering, Key Laboratory for Polymeric Composite and Functional Materials of Ministry of Education, Sun Yat-sen University, Guangzhou 510275, China*

[b] *Beijing Synchrotron Radiation Facility, Institute of High Energy Physics, Chinese Academy of Sciences, Beijing 100049, China*

[c] *University of Chinese Academy of Sciences, Beijing 100049, China*

[d] D*epartment of Chemistry, Saarland University, 66123, Saarbrücken, Germany*

[*]Corresponding authors' contact: liuzh287@mail.sysu.edu.cn (Z. L.), zhangpeng3@mail.sysu.edu.cn (P.Z.)

ABSTRACT

In this work, post-treatment-free polymer hybrids, consisting of poly(3,4-ethylenedioxythiophene):poly(styrene sulfonate) (PEDOT:PSS) and ionic liquids (ILs), were fabricated for the thermoelectric (TE) application. By optimizing the ILs' molar concentration (0-0.5 M) and chemical composition, that is varying the cyano-based anions coupled with 1-ethyl-3-methylimidazolium cations, a superior TE performance (power factor of 190 μW m^{-1} K^{-2}) was achieved. The excellent TE performance was attributed to the conductive network under the coupling effect of molecular structure (such as oxidation level, conformation and crystallization of PEDOT chains) and microstructure (long-range ordered conductive paths). Especially, the long-range conductive paths were proved to be made of rod-like microdomains, based on detailed structure analysis with micro-Fourier transform infrared spectroscopy and small-angle X-ray scattering. These paths enabled carrier transport among microdomains of PEDOT:PSS/IL hybrids. Moreover, the conductive network of PEDOT:PSS/IL hybrids showed good environmental and mechanical stability, enabling the fabrication of flexible TE generators.

KEYWORDS: PEDOT:PSS, ionic liquid, thermoelectric, post-treatment-free, structure-property correlation

1. Introduction

Thermoelectric generator (TEG) is a sustainable and ecofriendly energy resource that can covert heat flux (e.g., waste energy) directly into electrical energy through the well-known Seebeck effect [1]. In the past decades, the development of high-performance TE materials have drawn extensive attention, which is believed to help mitigate the challenges of global energy dilemma [2,3]. The performance of TE materials is evaluated with a dimensionless figure-of-merit (ZT), defined as $ZT = S^2\sigma T/\kappa$, where S, σ, T and κ stands for Seebeck coefficient, electrical conductivity, absolute temperature and thermal conductivity, respectively. Recently, conducting polymer-based TE materials attract great interests since their merits in low cost, non-toxic, large-scale processability, intrinsic flexibility and low κ values, which fit well to the development trend of electronics towards integration, miniaturization and super flexibility [4,5]. Especially, the κ value of polymer materials is so low (0.1–1 W m^{-1} K^{-1}) [6] that is difficult to be measured precisely. Therefore, the TE performance of polymer-based materials is usually qualified by $S^2\sigma$, called power factor (PF) [7]. Moreover, like their inorganic counterparts, the polymer-based TE materials generally follow a tradeoff relationship, in which a higher S value is coupled with a lower σ value. In order to get out of the dilemma, the research greatly focus is on how to decouple the S and σ by tailoring the structure via synthesis, secondary-doping or post-treatments, to achieve their synergistic enhancement [4,5,8,9].

By referring to the previous reports, poly(3,4-ethylenedioxythiophene):poly (styrene sulfonate) (PEDOT:PSS), a complex of conducting PEDOT doped with insulating PSS, has drawn the most attention [4]. This is because its remarkable stability in ambient conditions and relatively higher conductivity compared to other polymers, as well as the biocompatible and environment benign aqueous wet coating capability [10]. The multilevel structure of the PEDOT:PSS has been intensively studied in the past decades, which is summarized in the following.

1. the primary *p*-type doping level of PEDOT during the oxidative polymerization is approximately 33%, that is 1 dopant for 3 monomer units [11] (Fig. 1a);

2. long and insulating PSS chains are covering around the short PEDOT chains (7-18 repeating unit [12]) via Coulombic interaction and in excess amount to guarantee the stability of the PEDOT:PSS aqueous dispersion;

3. PEDOT-rich core and PSS-rich shell microstructure forms in the aqueous dispersion due to the preferential proximity between water and hydrophilic PSS chains [13];

4. Supramolecular assembly formed already in the solution, which has strong correlations with the structure (such as crystallinity, interdomain connectivity) and electrical property of the dried film [14-16].

The above-mentioned structure features endow PEDOT:PSS localized carriers (Fig. 1a) and thus the carrier transport heavily relying on interchain and intergrain transfer, for which ordered structure in multilevel is mandatory [5,8,10,17]. In the past decades, the structure and morphology of the PEDOT:PSS have very often been scrutinized based on different approaches such as optimized polymerization, secondary doping and post-treatments, to understand the inherent transport mechanisms [4]. A three-fold increase in the conductivity was widely reported via pre- or post-treatments with doping agents like acids [18,19], salts [20], surfactants [21], and organic solvents [22,23]. The conductivity enhancement was mainly attributed to the coupling effect of the more ordered PEDOT microstructure and minimized content of the insulating PSS components [24,25].

It is found that secondary doping with ionic liquids (ILs) overcome the thermoelectric tradeoff relation of PEDOT:PSS. For example, Kee et al reported that the IL-doped PEDOT:PSS showed superior S and σ performances simultaneously over neat PEDOT:PSS, i.e., 538 S cm^{-1} Vs. 1 S cm^{-1} and 25 μV K^{-1} Vs. 15 μV K^{-1} [26]. Ju et al explained such tradeoff break phenomenon with a hypothesis that change of the electrostatic interaction between PEDOT:PSS and secondary dopant induced substantial structure change and a positive deviation from the TE tradeoff relation [14]. In addition, Fan et al. demonstrated that IL doping combined with post-treatments with H_2SO_4 and NaOH could endow PEDOT:PSS heterostructures and high TE performance (PF=754 μW m^{-1} K^{-2}) [27]. Moreover, Hinckley et al. reported that the well-designed solution-shearing deposition combined with solvent post-treatments brought PEDOT:PSS metallic-like conductivity and high PF (> 800 μW m^{-1} K^{-2}) performance, which were attributed to the PEDOT chain alignment and increased microdomain size during the process [28]. However, these post-treatment protocols usually involve complex and cumbersome processing steps, some of them even need toxic and dangerous chemicals, which might bring obstacles for the large-scale production of PEDOT-based TE and their applications.

In this work, we prepared a series of post-treatment-free PEDOT:PSS/IL hybrid and studied their TE performance as a function of the chemical structure and concentration of the IL dopants. We disclosed that a balanced molecular structure and microstructure was necessary for the optimum of TE performance. Four ILs with the same 1-ethyl-3-methylimidazolium (EMIM) cation but different cyano-based anions, including thiocyanate

(SCN), dicyanamide (DCA), tricyanomethanide (TCM) and tetracyanoborate (TCB) were chosen in the study. A superior PF value of 190 μW m^{-1} K^{-2} was first reported in the PEDOT:PSS/EMIM:SCN 0.25 sample. To the best of our knowledge, it's the highest performance ever reported in the post-treatment-free PEDOT-based TEs. To rationalize this phenomenon, sophisticated and complementary characterization techniques have been undertaken to decipher the multiple-length scale structure covering both molecular structure (the oxidation level, conformation and packing of the PEDOT chains) and microstructure (long-range ordered conductive paths consisting of rod-like microdomains). Especially we demonstrated that the establishment of long-range conductive paths except for the well-recognized optimized molecular structure [5,7,8] played important roles in the high TE performance. Moreover, the TEG was fabricated and tested to demonstrate the promising practical applications of these post-treatment-free PEDOT/IL hybrid.

2. Results and Discussion

2.1. Materials Design and Property

We designed the post-treatment-free *w*/IL (where *w* denotes the PEDOT:PSS) TEs by referring to the fundamentals disclosed in the previous studies. To name a few, chemical structure of the ILs determines the doping efficiency and has strong impact on the performance of the PEDOT-based TEs [29,30]. An increase in carrier density might yield lower carrier mobility, indicating the existence of an optimum concentration for the IL dopants [31,32]. It's natural to understand that rational design of the chemical structure and concentration of ILs determines the high performance *w*/IL TEs. By surveying the literature reports, the ILs with EMIM cations were chosen since they were intensively studied as the secondary dopant or post-treatment solvent in the PEDOT-based TEs [33], and their commercial availability. In addition, four cyano-based anions (Fig. 1a) were chosen as the counterions of EMIM, for a systematic study of the role of chemical structures. Inspired by one of our recent work [15], which disclosed that the *w*/EMIM:TCM 0.17 (where 0.17 is the molar concentration of EMIM:TCM) showed an optimized PF of 175 μW m^{-1} K^{-2}, we set the molar concentration of IL (*n*) in the range of 0-0.5 M in this study.

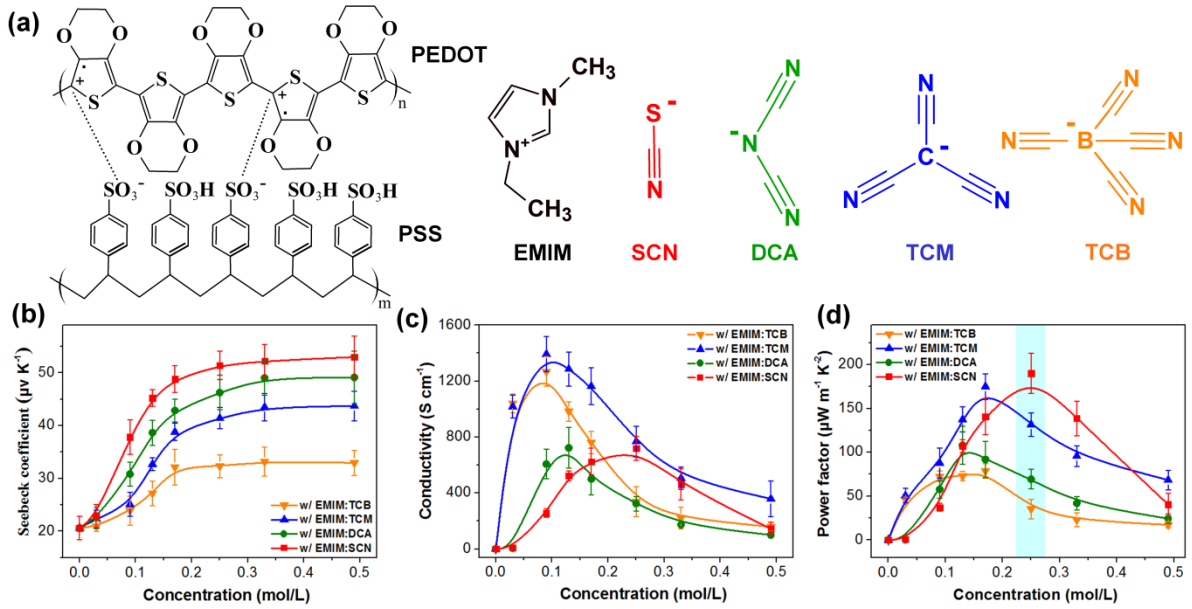

Fig. 1. (a) Chemical structures of PEDOT:PSS and ILs used in this work. (b) Seebeck coefficient, (c) electrical conductivity and (d) power factor of PEDOT:PSS/IL (denoted as *w*/IL) hybrid films as a function of the ILs' concentration (*n*). In panel d, the *w*/IL with optimum PF value was marked with color bar. In panels b-d, the solid lines are guides to the eye.

Fig. 1b shows that the *S* values of all the *w*/IL samples increase logistically with the increase of *n*; for the fixed *n* value, the *S* values show clear anion dependency with SCN > DCA > TCM >TCB. For example, *w*/EMIM:SCN reaches a maximum $S = 51.4$ μV K^{-1} at $n \geq 0.25$ M, which is 2.5 time higher than that of pristine PEDOT:PSS (20.6 μV K^{-1}). In contrast, the change of σ value as a function of *n* is more complex. With the increase of *n*, σ increases first and then decreases with the maxima in the middle as shown in Fig. 1c. The *w*/EMIM:TCM shows the highest σ value of 1393 S cm^{-1}, three orders higher than that of neat PEDOT:PSS (0.85 S cm^{-1}). By comparing Fig. 1 b and c, a clear tradeoff relationship between *S* and σ is found at high *n* values. Therefore, to fabricate the high performance TE, it's ideally to get both *S* and σ at maxima in the sample by following the function PF= $S^2\sigma$. Indeed, the *w*/EMIM:SCN 0.25 fits well to the condition with S = 51.4 μV K^{-1} and σ = 719 S cm^{-1}, resulting in a superior PF value of 190 μW m^{-1} K^{-2} (Fig. 1d). In addition, Fig. 1d shows that the *PF* performances of all the *w*/IL samples have clear dependence on the chemical structure and concentration of the IL dopants. For example, at n = 0.25 M, the *w*/EMIM:SCN shows an overall best PF, which is higher than that of *w*/EMIM:TCM (132 μW m^{-1} K^{-2}), *w*/EMIM:DCA (69 μW m^{-1} K^{-2}) and *w*/EMIM:TCB (35 μW m^{-1} K^{-2}). By comparison, the TE performance of *w*/EMIM:SCN 0.25 is higher than not only the other samples used in this work but also the previously reported PEDOT:PSS hybrids doped with ILs [26,34,35], dimethyl sulfoxide [36],

hydrazine [37], ethylene glycol [38], polyethylene glycol [39], and some inorganic fillers [40-44]. More details could be found in Fig. S1 of the Supporting Information. To explore the underlying principles of the new record, we did an exemplary study of the structure and property correlation with *w*/IL 0.25 samples from the perspective of balanced molecular and microscopic structures in the following.

2.2. Molecular Structure

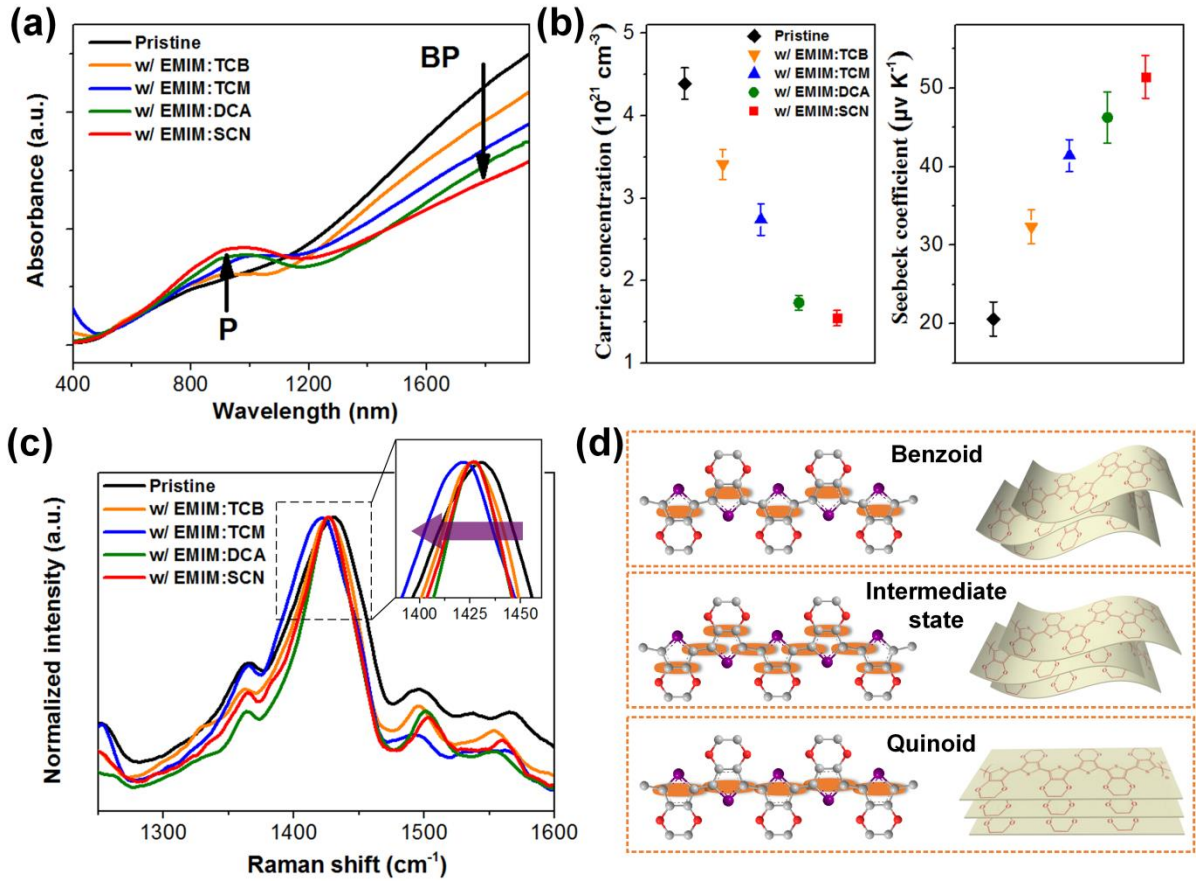

Fig. 2. (a) UV−vis-NIR absorbance spectra of *w*/IL 0.25 hybrid films. The arrows are guides to the eye for change of polaron (P) and bipolaron (BP) peak intensities. (b) Charge carrier concentration and Seebeck coefficient results of *w*/IL 0.25 hybrid films. (c) Raman spectra of the *w*/IL 0.25 hybrid films. The signal around 1425 cm^{-1} is zoomed and included as an inset, with an arrow indicates the peak shift direction as a function of IL. (d) Schematic diagrams showing the resonant characters and the planarity of the π-π stacking in the *w*/IL hybrid. The C = C double bonds are marked with golden rectangular shades.

As well-recognized in the literature, the molecular structure of conjugate polymer has strong impact on the TE performance [4]. The molecular structure of the *w*/IL 0.25 samples were characterized with UV-vis-NIR, Raman spectroscopy and X-ray scattering, which can provide splendid information about oxidation level, conformation and packing states of PEDOT chains. The UV-vis-NIR spectroscopy data of *w*/IL 0.25 samples (Fig. 2a) show typical polaron and bipolaron signal of PEDOT at around 900 and 1200 nm, respectively [45-

47]. By comparing to the pristine PEDOT:PSS sample, the *w*/IL 0.25 samples exhibit a clear increase in the polaronic absorption and a concomitant decrease in the bipolaronic absorption, indicating that IL doping generally reduced the oxidation level of PEDOT. The level of the reducing effect is closely related to the chemical structure of the IL and increases in the sequence of TCB < TCM < DCA < SCN. In addition, the reduction effect is positively correlated with the concentration of ionic liquid (as testified by UV-vis data in Fig. S2 of the Supporting Information). Moreover, it's generally accepted that the oxidation level has a positive dependence on the charge carrier concentration, vice versa for the Seebeck coefficient [29,45]. Similar phenomenon has been observed in the *w*/IL 0.25 samples as shown in Fig. 2b. Note: the charge carrier concentration was collected with Hall effect measurement. By referring to the ion exchange theory between PEDOT:PSS and ILs [30], these phenomena could be rationalized with the fact that the smaller anion could easily penetrate the coupled PEDOT:PSS chains, resulting the dissociation of PEDOT from PSS segments, as schematically illustrated in Fig. S3 of the Supporting Information.

The molecular conformation of PEDOT was characterized via Raman spectroscopy. Fig. 2c shows that pristine PEDOT:PSS has a Raman peak at 1430 cm^{-1}, which is assigned to the symmetric C_α=C_β stretching vibrations of PEDOT rings [48]. IL doping causes peak narrowing, corresponding to de-doping of PEDOT [14]. This finding agrees well with the UV-vis-NIR results as mentioned above. In addition, IL-doping brings red-shift of the peak position, that is 1422 and 1427 cm^{-1} for *w*/EMIM:TCM sample and the other samples, respectively. This phenomenon can be correlated with the resonant characters (benzoid, intermediate and quinoid structure) of PEDOT [16]. As illustrated in Fig. 2d, the benzoid and quinoid structures exist in distorted and ordered PEDOT backbones, respectively. Moreover, a high proportion of quinoid structure brings the PEDOT chain longer conjugation length, promoting the π-π stacking among PEDOT chains and crystallization to some extent [49]. To testify this hypothesis, we characterized the chain packing and crystallization of *w*/IL 0.25 samples with X-ray scattering in the next part.

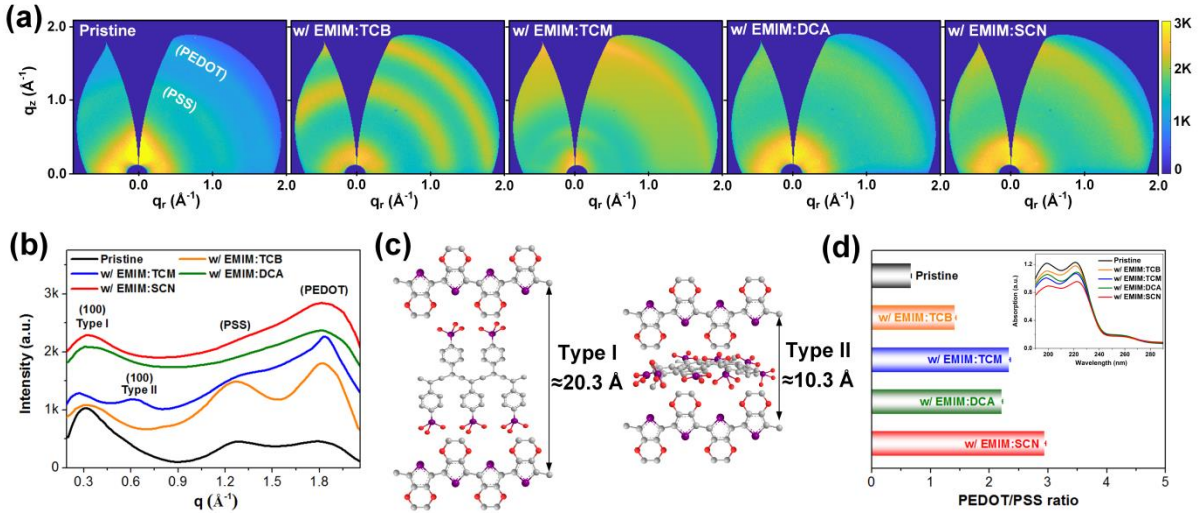

Fig. 3. GIWAXS data of the *w*/IL 0.25 hybrid films: (a) typical 2D GIWAXS (after wedge correction) patterns and (b) corresponding 1D GIWAXS profiles integrated along cake cuts. (c) Schematic diagram of the (100) lamellar stacking structures of PEDOT:PSS, extracted from the GIWAXS data. (d) PEDOT-to-PSS ratios of the sample extracted by dividing the PEDOT peak intensity with that of PSS as marked in Panel b. The inset depicts the UV-vis results of PEDOT:PSS films.

Grazing-incidence wide-angle X-ray scattering (GIWAXS) is a well-established powerful protocol in providing statistic molecular structure information of polymer thin films [14,24,50-53] in large-area, which is determined by the beam footprint. For example, Palumbiny et al. deciphered how solvent additives influence PEDOT:PSS thin film in terms of interchain coupling, molecular orientation, and crystallite size based on GIWAXS measurements [50]. Fig. 3a shows the typical 2D GIWAXS patterns that have been corrected for the "missing wedge". Two halo rings observed at high q region (Fig. 3a) are attributed to the π-π stacking of PEDOT and PSS chains, respectively. In the low-q region, scattering patterns resulting from interchain coupling are also observed, varying with the change of ILs. To qualitatively analyze the structure change, the 2D GIWAXS patterns were converted into 1D profiles (Fig. 3b) by cake integration (cf. Fig. S4 of the Supporting Information). Three scattering peaks were found in pristine PEDOT:PSS, with q = 0.31, 1.26 and 1.79 Å^{-1}. By referring to $d = 2\pi/q$, these peaks correspond to real-space values d = 20.27, 4.99 and 3.51 Å, respectively. The latter two peaks were attributed to the π-π stacking of PSS and PEDOT chains (Figure 3b), respectively. Meanwhile, the first peak was attributed to the (100) crystalline peak of PEDOT, that was alternating stacking of PEDOT and PSS as illustrated in Fig. 3c (type I) [24,50]. It's found that the position of the PEDOT (100) peak does not change with the IL-doping except for *w*/EMIM:TCM 0.25. Two peaks with q = 0.27 and 0.61 Å^{-1} (d = 23.27 and 10.30 Å) are found in *w*/EMIM:TCM 0.25 sample (Fig. 3b), which are attributed to

a peak shift of type I and formation of a new type of PEDOT (100) structure (type II in Fig. 3c), respectively [19]. As shown in Fig. 3c, the type II structure minimized the intermolecular gaps of PEDOT chains, which was demonstrated to facilitate the charge transport and to improve the electron conductivity [19]. Indeed, as shown in Fig. 1c, EMIM:TCM doped sample showed the highest σ value in the *w*/IL 0.25 series sample. The formation of type II PEDOT (100) structure could be rationalized with the high proportion of quinoid structure in *w*/EMIM:TCM (Fig. 2 c and d), which would promote the π-electronic overlap and the transport of charge carriers [14,54,55].

It's well-known that GIWAXS could not only provide splendid molecular structure information of polymer chains but also their statistics in a large area [52,53], that is the beam footprint (0.7×45.8 mm^2 in the present work, schematic diagram in Fig. S5 of the Supporting Information). The statistic result provides PEDOT to PSS ratio information, which is closely related with the σ performance because PEDOT is conductive and PSS is insulating [56]. By referring to the literature [19], the PEDOT to PSS ratios was calculated by comparing the scattering peak intensities of PEDOT and PSS as indicated in Fig. 3b. Note: the peak position might shift due to the structure fluctuation and detailed information about the peak position could be found in Table S1 of the Supporting Information. Fig. 3d shows that the PEDOT to PSS ratio increases significantly by IL-doping in the drop-casted samples, in the sequence of EMIM:SCN > EMIM:TCM > EMIM:DCA > EMIM:TCB. Similar phenomenon has been observed in the UV-vis data of the spin-coated samples (inset of Fig. 3d). In the UV-vis spectra, the two absorption peaks around 210 nm are attributed to the PSS aromatic ring signal [57], and the decrease of the intensity indicates the minimizing of the PSS relative content. It has been demonstrated that the PSS could be washed away via post-treatments because it can be decoupled with PEDOT after secondary doping and it has much better solubility than PEDOT [29,58]. However, it is not the case for the samples in the present study since drop-casted samples were used for the GIWAXS measurements and no PSS wash-away was expected. Instead, we attribute the results in Fig. 3d to the more ordered π–π stacking of PEDOT in the scanned area since ordered structure except for the number of the scatter could enhance the scattering intensity [50,51]. Moreover, the statistic structure analysis results indicate the *w*/EMIM:SCN has the best overall structure order; in contrast, the chemical structure analysis shows the *w*/EMIM:TCM has the most efficient chain packing in the crystal. Clearly, solely molecular structure information as mentioned above is not convincing in rationalizing the structure and property correlations of PEDOT-based TEs. In the following section, we decipher the microstructure of *w*/IL 0.25 samples with X-ray

scattering and micro-FTIR spectroscopy, to provide a comprehensive understanding of the structure and property correlation.

2.3. Microstructure

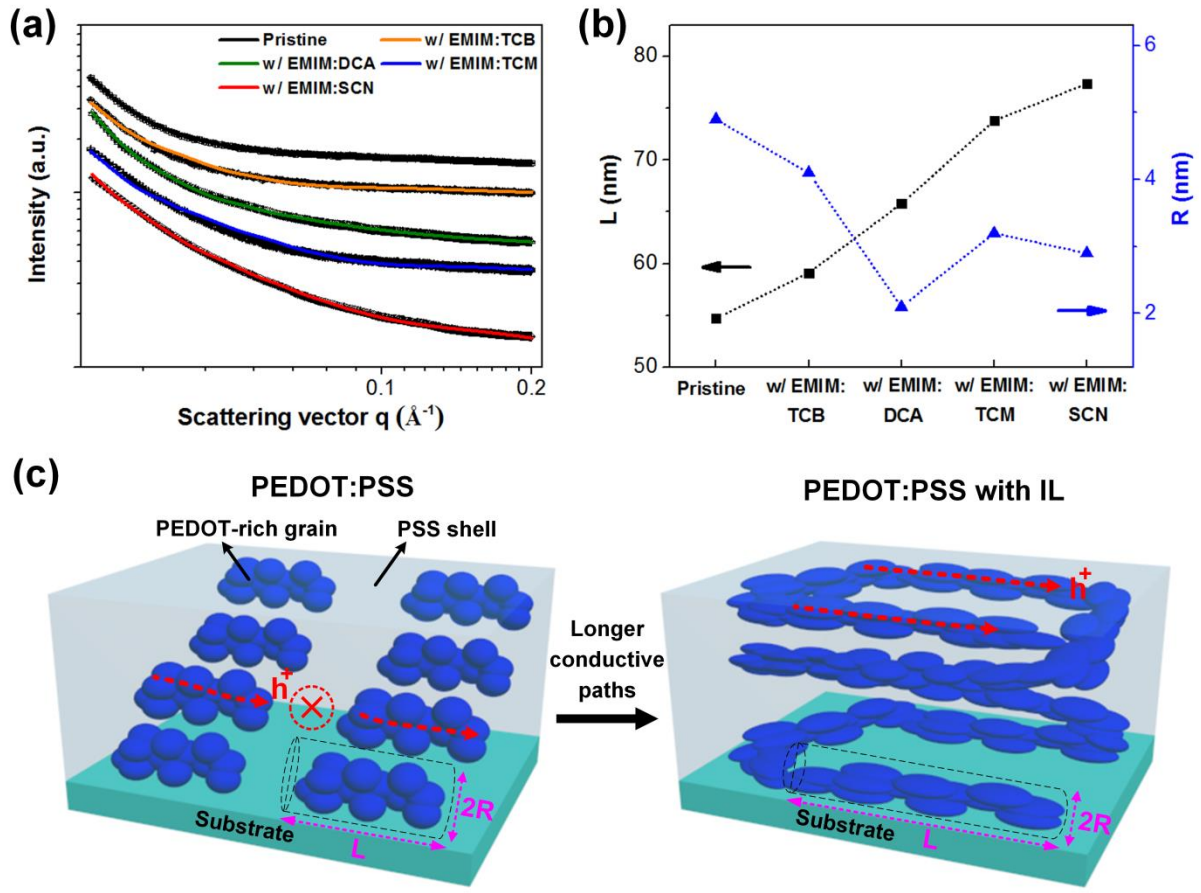

Fig. 4. (a) SAXS data (dotted lines) of *w*/IL 0.25 hybrid films and their model fits (solid lines). (b) Characteristic radii (R) and length (L) from the SAXS data fitting. (c) Schematic illustration of the IL doping induced microstructure change in PEDOT:PSS hybrids. The possible carrier (h^+) transport paths are indicated with dashed-line arrows.

Fig. 4a shows the synchrotron radiation small-angle X-ray scattering (SAXS) data of the *w*/IL 0.25 hybrid films. A schematic diagram of the SAXS measurement could be found in Fig. S6 of the Supporting Information. SAXS is a powerful tool in providing statistic microstructure information (like size, shape and assembly) of polymer, nanoparticles and so on in solution or solid state [14,59-63]. For example, Ju et al. demonstrated that the secondary doping switched the microstructure of PEDOT:PSS from original "core-shell" structure to a rod-like structure (PEDOT enriched in the center), based on the SAXS data [14]. The formation of such rod-like microstructures is generally observed in the IL-doped PEDOT:PSS samples and could enhance the materials' conductivity [8,15,28]. For a qualitative analysis of

the SAXS data, we fitted them with a rod-like model, and the characteristic radii (R) and length (L) values from the SAXS data fitting are shown in Fig. 4b. By comparison, the fitted L of pristine PEDOT:PSS (~ 55 nm) argreed well with the microdomain size of PEDOT:PSS mentioned in the previous report [16]. Fig. 4b shows that the L values increased clearly after IL-doping, in the sequence of EMIM:SCN > EMIM:TCM > EMIM:DCA > EMIM:TCB. Meanwhile, the fitted R values decreased after IL-doping, indicating the slender feature of the rod-like structure enhanced. By referring to the previous studies [25,27], such rod-like structures would promote the conductive network percolation and promote the intergrain carrier transport. The proposed microstructure and property correlations before and after IL doping are schematically illustrated in Fig. 4c.

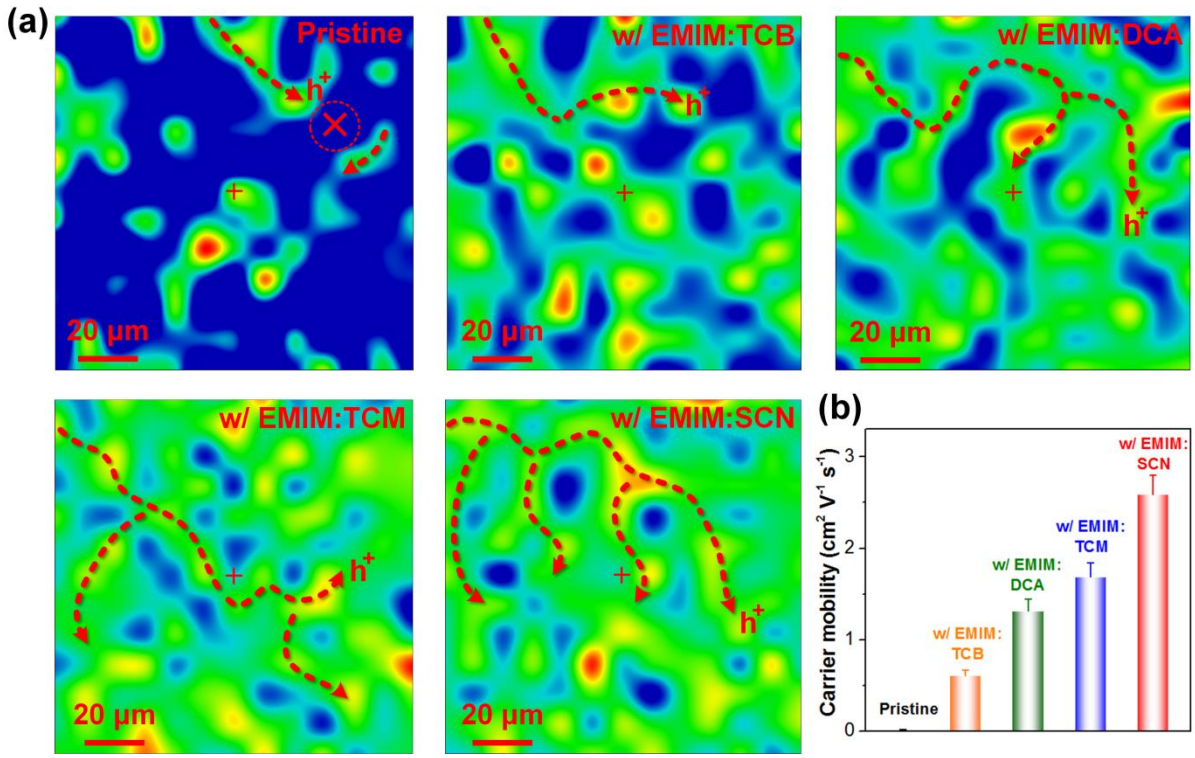

Fig. 5. (a) μ-FTIR mapping data of *w*/IL 0.25 hybrid films, showing the intensity distribution of the 832 cm^{-1} peak (PEDOT). The data is in rainbow color with red and blue indicate rich and deficient of PEDOT. The dashed-line arrows guide eyes to judge the formation of long conductive paths for carrier (h^+) transport in the sample. (b) Charge carrier mobility (μ_0) results of the *w*/IL 0.25 hybrid films, which were collected from Hall effect measurement.

To provide more solid proof about the proposed conductive network, the micro-Fourier transform-infrared spectroscopy (μ-FTIR) was employed. μ-FTIR combines spectral characterization of FTIR with spatial resolution of light microscopy, which can provide spectroscopic information of the conductive domains with micrometer range spatial resolution

[64]. PEDOT is conductive and its chemical structure is conveniently analyzed with FTIR as mentioned in the previous report [65]. To study the spatial distribution of PEDOT in the film (cf. Fig. S7 of the Supporting Information), the 832 cm^{-1} peak signal, assigned to the stretching vibration of C-S-C in the thiophene ring [66], was chosen for the μ-FTIR mapping analysis. The μ-FTIR data was shown in rainbow color, with red and blue indicate rich and deficient of the PEDOT, respectively. Fig. 5a shows that isolated PEDOT-rich microdomains are scattering over the pristine PEDOT:PSS; the IL-doping promotes the percolation of the PEDOT-rich microdomains, that is formation of long-range ordered conductive paths (LOCP) as indicated by the dashed-line arrows. By comparison, the integrity of the LOCP decreases in the order of EMIM:SCN, EMIM:TCM, EMIM:DCA, EMIM:TCB and pristine PEDOT:PSS. The formation of LOCP would pave ways for the carrier transport, as evidenced in the charge carrier mobility (μ_0) data of Fig. 5b. Considering these are post-treatment-free samples, we attribute the formation of such LOCP structure in the dried films to the structure transfer from those formed in the solution due to supramolecular assembly as illustrated in the previous reports [15,30]. By comparing Fig. 5 a and b, it is found that the change of μ_0 as a function of IL species is the same with that of the integrity of the LOCP. In addition, they agree well with structure analysis mentioned above, that is rod-like structure (Fig. 4) and PEDOT to PSS ratio in large area (Fig. 3d). Moreover, they agree with the Seebeck coefficient (Fig. 2b) and TE performance (PF value in Fig. 1d), too. Thus, we confirm that the microstructure except for the well-known chemical structure plays important role in performance of PEDOT-based TEs.

It's well known that high performance TE materials need both high carrier transport properties and low phonon transport properties simultaneously, which makes it challenge to enhance thermoelectric performance [67]. We attribute the new record PF value of *w*/EMIM:SCN 0.25 to the conductive network with balanced microstructure and molecular structure. For one side, the *w*/EMIM:SCN 0.25 has one of the highest *S* values (Fig. 1b), which is supported by the best integrity of the long-rang ordered conductive path. For the other side, it has good σ (Fig. 1c) due to the balance of molecular structure and long-range ordered conductive path. In addition, it was found that the conductive network formed in *w*/IL 0.25 samples showed good environmental stability (cf. Fig. S8 of the Supporting Information). For example, the PF value of *w*/EMIM:SCN 0.25 sample showed much better environmental stability (83.4% retention after 10 days) than that of pristine PEDOT:PSS (i.e., 58.6% retention), promising for the potential applications in TEG.

2.4. Thermoelectric Generator

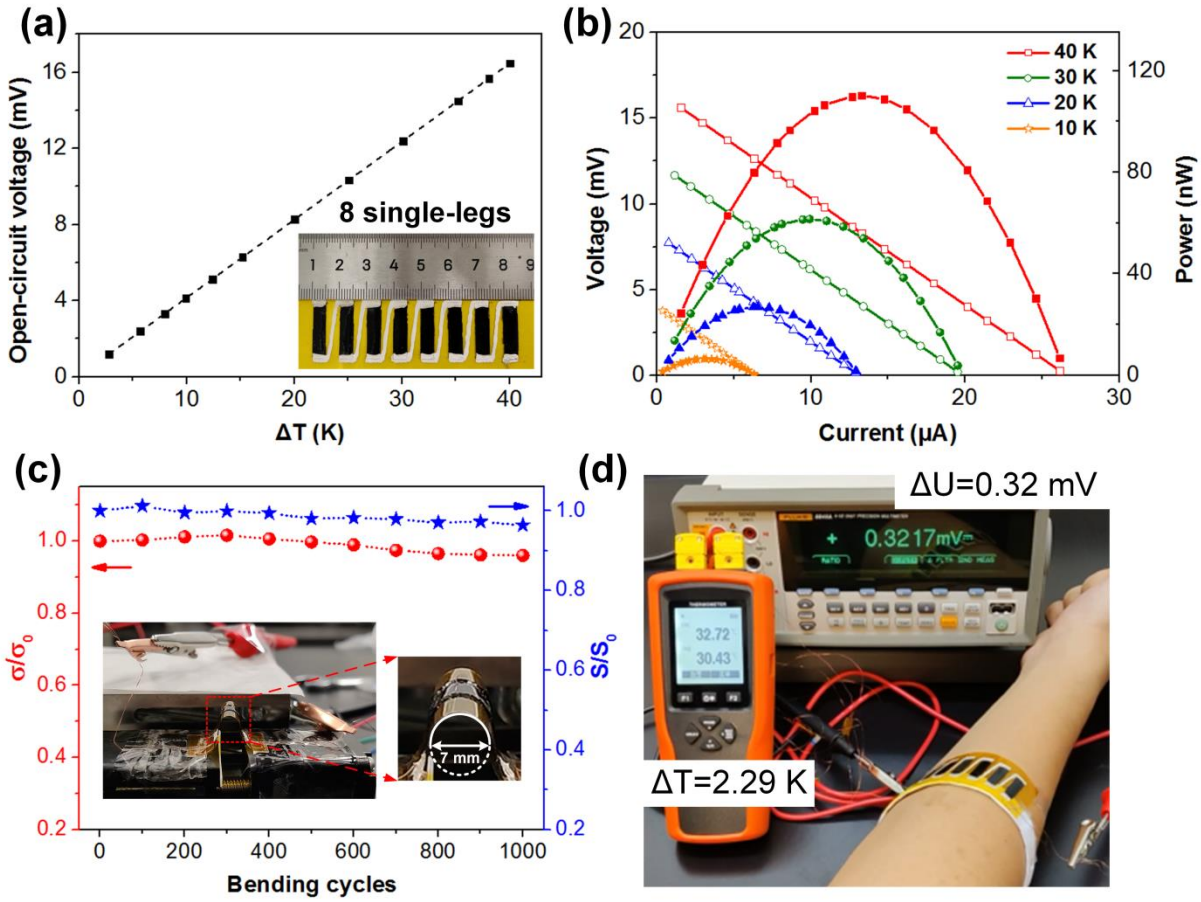

Fig. 6. Performance evaluation of TEG fabricated with *w*/EMIM:SCN 0.25 as the TE material. (a) The relationship between output voltage and the temperature gradient (ΔT). The inset is a photo image of the 8 p-type legs TEG. (b) Output voltage (hollow dot) and output power (solid dot) versus current at different ΔT. (c) Electrical conductivity and Seebeck coefficient as a function of bending cycles. The inserted photo images showing the configuration of operando study during bending test. (d) A photo of ~0.32 mV created when ΔT was 2.29 K. The flexible TEG was wrapped around the arm with one side attached to an arm skin and the other side exposed to the air, air-laid paper as the thermal insulator.

To explore the application of the *w*/IL in TE device, we fabricated 8-legs TEG (inset of Fig. 6a) with the p-type *w*/EMIM:SCN 0.25 sample. Fig. 6a shows the open-circuit voltage (V_{oc}) of the TEG is 16.5 mV when temperature gradients (ΔT) is 40 K. The V_{oc} value is close to the theoretically estimated value (16.6 mV), with the equation $V_{oc} = N \cdot S \cdot \Delta T$ (N represents the number of legs, S measured from a single TE leg), indicating good electrical circuit formed in the TEG. Fig. 6b shows the output performance of the TEG as a function of load resistance at different temperature gradient, as schematically illustrated in Fig. S9 of the Supporting Information. The output power (P) is described by the equation: $P = [V/(R_I + R_L)]^2 R_L$, where R_I and R_L represent the intrinsic internal resistance and the load resistance, respectively. Therefore, P reaches its maximum when R_I equals to R_L at a fixed ΔT [68]. The R_I was 625 Ω. Fig. 6b shows that the P increases from 6.4 to 110.2 nW when ΔT changes

from 10 to 40 K, indicating good TE performance of the TEG.

The PEDOT-based TEG is a typical flexible TEG due to the excellent flexibility [4]. To address this point, bending measurement of single leg was undertaken. The bending diameter was set to 7 mm (inset of Fig. 6c). Fig. 6c shows the PEDOT-based TEG retains the TE performance about 96.0% of the original σ and 96.4% of the original S, after 1000 bending cycles. By calculation, the PF decreases 10.7% after 1000 times bending, attractive for the practical applications. To demonstrate the practical application of such device, the 8-legs TEG was wrapped around the arm, to generate electricity with body heat. As shown in Fig. 6d, good contact between TEG and skin was achieved with one side attached to the arm and the other side exposed to air with an air-laid paper as the thermal insulator. The resulting open-circuit voltage of the TEG was 0.32 mV at a temperature difference of 2.29 K. This finding promotes the post-treatment-free *w*/IL hybrids towards practical applications in harvesting human body heat.

3. Conclusions

In this work, we demonstrated a strategy to prepare high-performance PEDOT-based TE materials by tailoring the chemical structure and concentration of the secondary dopants. A high PF value of 190 μW m^{-1} K^{-2} with simultaneously enhanced S and σ performance was achieved at *w*/EMIM:SCN 0.25 sample. The superior performance was attributed to the conductive network with balanced microstructure and molecular structure. The combination of SAXS and μ-FTIR evidenced the conductive network with long-range ordered conductive paths (LOCP) consisting of packed rod-like microdomains. We first addressed that the integrity of these LOCP determined the materials' TE performance except for the well-known chemical structure. Moreover, the strategy was based on a post-treatment-free solution coating protocol, which can be easily adapted to the large-scale device fabrication with the established industry-scale techniques. Furthermore, we demonstrated the application of the *w*/EMIM:SCN 0.25 materials in the application of flexible TEG, which generated electricity by harvesting human heat. All these findings are expected to promote the design and production of high-performance flexible TEGs and their commercial applications.

4. Experimental Section

4.1. Materials. PEDOT:PSS solid pellets (Orgacon Dry) were purchased from Agfa Gevaert N.V., Belgium. 1-ethyl-3-methylimidazolium thiocyanate (EMIM:SCN) and 1-ethyl-3-methylimidazolium dicyanamide (EMIM:DCA) were purchased from Lanzhou Institute of Chemical Physics, Chinese Academy of Sciences, China. 1-ethyl-3-methylimidazolium

tricyanomethanide (EMIM:TCM) was purchased from TCI Chemical Industry Development Co., Ltd (Shanghai, China). 1-ethyl-3-methylimidazolium tetracyanoborate (EMIM:TCB) was synthesized based on the protocol mentioned in the previous work [24]. Distilled water was purchased from Watsons (Guangzhou, China). Glass slides (size: 24 mm × 24 mm) were purchased from Aladdin Bio-Chem Technology Co., LTD (Shanghai, China). Silicon wafer ((100) orientation) was purchased from PlutoSemi Co., Ltd., and used by cutting into small pieces.

4.2. Sample Preparation. PEDOT:PSS solid pellets were mixed with distilled water to form 1.3 wt% PEDOT:PSS aqueous dispersions after thorough stirring. Afterwards, ILs were added to 1 mL of PEDOT:PSS aqueous dispersion at set molar concentration values (i.e., 0.03, 0.09, 0.13, 0.17, 0.25, 0.33 and 0.49 M), to get the PEDOT:PSS/IL hybrid solution after vigorously stirring. Note that PEDOT:PSS/IL hybrid was denoted as *w*/IL *n* where *n* indicated the molar concentration of IL. Typically, w/EMIM:TCB 0.25 indicates the PEDOT:PSS mixes with 0.25 M EMIM:TCB. The glass slides or silicon substrates were first cleaned with a commercial detergent solution and then sequentially sonicated in distilled water, acetone and ethanol for 10 min each. For the thin film sample preparation, the w/IL solutions were placed onto glass slides or silicon substrates that first spread at 400 rpm for 18 s and then spin-coated at 1000 rpm for 60 s, and finally dried under ambient condition (temperature 25 °C and humidity 65% RH). About 200 μL of the as-prepared *w*/IL samples were drop casted on the dried glass substrates and silicon wafers for conductivity and X-ray measurements, respectively. In addition, the TEG was fabricated by drop-casting the *w*/IL solution onto the Kapton film in rectangular shape as n-type legs, which were connected with silver inks and copper wires (Fig. 6).

4.3. Characterization. Seebeck coefficient (*S*) measurements were performed at room temperature with a home-made Peltier heater to control the sample temperature and a Fluke multimeter 8846A to collect the thermovoltage. In brief, the *S* value was estimated from the slope of the linear relationship between thermoelectric voltage and the temperature difference of the probes, as schematically illustrated in Fig. S10 of the supporting information. Silver paste (around 1 mm) was top dotted onto the polymer, to stabilize the contact between probes and polymer film, as mentioned in our recent work [15]. The electrical conductivity was measured with a digital multimeter (RTS-8, Guangzhou Four Probe Technology Co., Ltd., China) by following the four-probe method. The relative humidity was approximately 65% during the conductivity and Seebeck coefficient measurements. The film thickness values were determined with a profilometer (Ambios XP-1, USA). The oxidation levels of the *w*/IL

samples in solution and dried-film states were characterized with a Lambda 950 (Perkin-Elmer) UV-vis-NIR spectrometer in transmission mode and a Maya 2000Pro (Ocean Optics) UV-vis spectrometer in reflection mode, respectively. The Raman spectra of the w/IL films were characterized with a Raman spectrometer (InVia, Renishaw), based on 1200 line/mm diffraction grating and 532 nm excitation wavelength. Carrier concentration and carrier mobility of the *w*/IL films were characterized with a Hall measuring system (HET-RT, JouleYacht Technology Co., Ltd.). Grazing-incidence wide-angle X-ray scattering (GIWAXS) with synchrotron light experiments were carried out at the 1W1A station of Beijing Synchrotron Radiation Facility (BSRF, China). The GIWAXS experiments were undertaken with a Huber 5-circle diffractometer and the scattered signal was collected with a 2D image plate (MAR-345, USA) at wavelength λ = 1.54 Å. The incident angle (α_i) and sample to detector distance (SDD) were set to 0.5° and 438 ± 1 mm, respectively. The SDD value was calibrated with a silver behenate standard. The beamsize was 0.7 × 0.4 ($H \times V$) mm^2, and the estimated beam footprint area was 0.7 × 45.8 mm^2. The GIWAXS data was analyzed with the GIXSGUI software package with the scattering vector $q = 4\pi \sin(\theta)/\lambda$. Cake cut of the 2D GIWAXS pattern was performed with the azimuthal range from -20° to 85° (with 0° being the polar direction of the detector plane). Synchrotron radiation small-angle X-ray scattering (SAXS) experiments were performed with drop-casted films on glass substrates at the BL19U2 station of Shanghai Synchrotron Radiation Facility (SSRF, China), with λ = 1.033 Å and SDD = 2210 ± 1 mm. The SAXS data was collected with a Pilatus 1M detector, and the 2D image was converted to 1D curve with a BioXTAS RAW software (version 1.6.3) after background correction, and the 1D data was fitted with a SASfit software package (version 0.94.10). The micro-Fourier transform infrared spectra (μ-FTIR) measurements were performed with an iS50 FTIR spectrometer (Thermo Scientific Nicolet, USA), in conjunction with a continuum infrared microscope and with a mercury cadmium telluride (MCT-A, 650 cm^{-1} cutoff) detector cooled with liquid nitrogen. The range of measurements was set from 4000 to 650 cm^{-1} at a spectral resolution of 8 cm^{-1}. The spectra were measured in reflection mode with 64 scan data averaging statistics and the beam aperture was 10 × 10 μm^2. The μ-FTIR measurements were made in the mapping mode, i.e., running individual measurements in a prespecified grid size (13 × 13 scan positions) in a chosen region of the sample. For the data analysis, the band of interest (that is 832 cm^{-1}) in the IR spectra was chosen for integration, and an intensity map was generated to show the intensity of the integrated band. Moreover, the intensity map was correlated back to its position in the measured grid.

Declaration of Competing Interest

The authors declare that they have no known competing financial interests or personal relationships that could have appeared to influence the work reported in this paper.

Acknowledgements

The authors acknowledge the financial supports from National Natural Science Foundation of China (No. 11905306 and U2032101), Fundamental Research Funds for the Central Universities (No. 19lgpy14) and "100 Top Talents Program" of Sun Yat-sen University. This work was carried out with the support of 1W1A beamline at Beijing Synchrotron Radiation Facility and 19U2 beamline at Shanghai Synchrotron Radiation Facility. We sincerely thank Prof. Dongbai Sun for his continuing support of this project and Ms. Yuxuan Li for her help during the sample preparation.

References

[1] X.-L. Shi, J. Zou, Z.-G. Chen, Advanced thermoelectric design: from materials and structures to devices, Chem. Rev. 120 (2020) 7399-7515.

[2] G.J. Snyder, E.S. Toberer, Complex thermoelectric materials, in: Materials for sustainable energy: a collection of peer-reviewed research and review articles from Nature Publishing Group, World Scientific. 2011, pp. 101-110.

[3] S.M. Pourkiaei, M.H. Ahmadi, M. Sadeghzadeh, S. Moosavi, F. Pourfayaz, L. Chen, M.A.P. Yazdi, R. Kumar, Thermoelectric cooler and thermoelectric generator devices: A review of present and potential applications, modeling and materials, Energy 186 (2019) 115849.

[4] S. Xu, X.-L. Shi, M. Dargusch, C. Di, J. Zou, Z.-G. Chen, Conducting polymer-based flexible thermoelectric materials and devices: From mechanisms to applications, Prog Mater Sci. 121 (2021) 100840.

[5] Y. Xu, Y. Jia, P. Liu, Q. Jiang, D. Hu, Y. Ma, Poly (3, 4-ethylenedioxythiophene) (PEDOT) as promising thermoelectric materials and devices, Chem. Eng. J. (2020) 126552.

[6] Z. Han, A. Fina, Thermal conductivity of carbon nanotubes and their polymer nanocomposites: A review, Prog Polym Sci. 36 (2011) 914-944.

[7] M. He, F. Qiu, Z. Lin, Towards high-performance polymer-based thermoelectric materials, Energy Environ. Sci. 6 (2013) 1352-1361.

[8] L. Deng, G. Chen, Recent progress in tuning polymer oriented microstructures for enhanced thermoelectric performance, Nano Energy 80 (2021) 105448.

[9] S. Wang, G. Zuo, J. Kim, H. Sirringhaus, Progress of conjugated polymers as emerging thermoelectric materials, Prog Polym Sci. (2022) 101548.

[10] M.N. Gueye, A. Carella, J. Faure-Vincent, R. Demadrille, J.-P. Simonato, Progress in understanding structure and transport properties of PEDOT-based materials: A critical review, Prog Mater Sci. 108 (2020) 100616.

[11] S. Kirchmeyer, K. Reuter, Scientific importance, properties and growing applications of poly (3, 4-ethylenedioxythiophene), J. Mater. Chem. 15 (2005) 2077-2088.

[12] P. Schmode, A. Hochgesang, M. Goel, F. Meichsner, J. Mohanraj, M. Fried, M. Thelakkat, A solution-processable pristine PEDOT exhibiting excellent conductivity, charge carrier mobility, and thermal stability in the doped state, Macromol Chem Phys. 222 (2021) 2100123.

[13] A. Elschner, S. Kirchmeyer, W. Lovenich, U. Merker, K. Reuter, PEDOT: principles and applications of an intrinsically conductive polymer, CRC press 2010.

[14] D. Ju, D. Kim, H. Yook, J.W. Han, K. Cho, Controlling electrostatic interaction in PEDOT:PSS to overcome thermoelectric tradeoff relation, Adv. Funct. Mater. 29 (2019) 1905590.

[15] X. Li, R. Zou, Z. Liu, J. Mata, B. Storer, Y. Chen, W. Qi, Z. Zhou, P. Zhang, Deciphering the superior thermoelectric property of post-treatment-free PEDOT:PSS/IL hybrid by X-ray and neutron scattering characterization, npj Flexible Electron. 6 (2022) 1-8.

[16] S. Tu, T. Tian, A.L. Oechsle, S. Yin, X. Jiang, W. Cao, N. Li, M.A. Scheel, L.K. Reb, S. Hou, Improvement of the thermoelectric properties of PEDOT:PSS films via DMSO addition and DMSO/salt post-treatment resolved from a fundamental view, Chem. Eng. J. 429 (2022) 132295.
[17] O. Bubnova, Z.U. Khan, H. Wang, S. Braun, D.R. Evans, M. Fabretto, P. Hojati-Talemi, D. Dagnelund, J.-B. Arlin, Y.H. Geerts, Semi-metallic polymers, Nat. Mater. 13 (2014) 190-194.
[18] F. Wu, P. Li, K. Sun, Y. Zhou, W. Chen, J. Fu, M. Li, S. Lu, D. Wei, X. Tang, Conductivity enhancement of PEDOT:PSS via addition of chloroplatinic acid and its mechanism, Adv. Electron. Mater. 3 (2017) 1700047.
[19] L. Bießmann, N. Saxena, N. Hohn, M.A. Hossain, J.G. Veinot, P. Müller-Buschbaum, Highly conducting, transparent PEDOT:PSS polymer electrodes from post-treatment with weak and strong acids, Adv. Electron. Mater. 5 (2019) 1800654.
[20] Z. Zhao, Q. Wu, F. Xia, X. Chen, Y. Liu, W. Zhang, J. Zhu, S. Dai, S. Yang, Improving the conductivity of PEDOT:PSS hole transport layer in polymer solar cells via copper (II) bromide salt doping, ACS Appl. Mater. Interfaces 7 (2015) 1439-1448.
[21] Z. Li, W. Meng, J. Tong, C. Zhao, F. Qin, F. Jiang, S. Xiong, S. Zeng, L. Xu, B. Hu, A nonionic surfactant simultaneously enhancing wetting property and electrical conductivity of PEDOT:PSS for vacuum-free organic solar cells, Sol Energ Mat Sol C 137 (2015) 311-318.
[22] L.V. Lingstedt, M. Ghittorelli, H. Lu, D.A. Koutsouras, T. Marszalek, F. Torricelli, N.I. Crăciun, P. Gkoupidenis, P.W. Blom, Effect of DMSO solvent treatments on the performance of PEDOT:PSS based organic electrochemical transistors, Adv. Electron. Mater. 5 (2019) 1800804.
[23] E. Hosseini, V.O. Kollath, K. Karan, The key mechanism of conductivity in PEDOT:PSS thin films exposed by anomalous conduction behaviour upon solvent-doping and sulfuric acid post-treatment, J. Mater. Chem. C 8 (2020) 3982-3990.
[24] S. Kee, N. Kim, B.S. Kim, S. Park, Y.H. Jang, S.H. Lee, J. Kim, J. Kim, S. Kwon, K. Lee, Controlling molecular ordering in aqueous conducting polymers using ionic liquids, Adv. Mater. 28 (2016) 8625-8631.
[25] X. Li, Z. Liu, Z. Zhou, H. Gao, G. Liang, D. Rauber, C.W. Kay, P. Zhang, Effects of cationic species in salts on the electrical conductivity of doped PEDOT:PSS films, ACS Appl. Polym. Mater. 3 (2021) 98-103.
[26] S. Kee, H. Kim, S.H.K. Paleti, A. El Labban, M. Neophytou, A.-H. Emwas, H.N. Alshareef, D. Baran, Highly stretchable and air-stable PEDOT:PSS/ionic liquid composites for efficient organic thermoelectrics, Chem. Mater. 31 (2019) 3519-3526.
[27] Z. Fan, D. Du, X. Guan, J. Ouyang, Polymer films with ultrahigh thermoelectric properties arising from significant seebeck coefficient enhancement by ion accumulation on surface, Nano Energy 51 (2018) 481-488.
[28] A.C. Hinckley, S.C. Andrews, M.T. Dunham, A. Sood, M.T. Barako, S. Schneider, M.F. Toney, K.E. Goodson, Z. Bao, Achieving high thermoelectric performance and metallic transport in solvent-sheared PEDOT:PSS, Adv. Electron. Mater. 7 (2021) 2001190.
[29] N. Saxena, B. Pretzl, X. Lamprecht, L. Bießmann, D. Yang, N. Li, C. Bilko, S. Bernstorff, P. Müller-Buschbaum, Ionic liquids as post-treatment agents for simultaneous improvement of Seebeck coefficient and electrical conductivity in PEDOT:PSS Films, ACS Appl. Mater. Interfaces 11 (2019) 8060-8071.
[30] A. de Izarra, S. Park, J. Lee, Y. Lansac, Y.H. Jang, Ionic liquid designed for PEDOT:PSS conductivity enhancement, J. Am. Chem. Soc. 140 (2018) 5375-5384.
[31] Q. Li, M. Deng, S. Zhang, D. Zhao, Q. Jiang, C. Guo, Q. Zhou, W. Liu, Synergistic enhancement of thermoelectric and mechanical performances of ionic liquid LiTFSI modulated PEDOT flexible films, J. Mater. Chem. C 7 (2019) 4374-4381.
[32] W. Shi, T. Zhao, J. Xi, D. Wang, Z. Shuai, Unravelling doping effects on PEDOT at the molecular level: from geometry to thermoelectric transport properties, J. Am. Chem. Soc. 137 (2015) 12929-12938.
[33] A. de Izarra, C. Choi, Y.H. Jang, Y. Lansac, Molecular dynamics of PEDOT:PSS treated with ionic liquids. Origin of anion dependence leading to cation design principles, The Journal of Physical Chemistry B 125 (2021) 8601-8611.
[34] A. Mazaheripour, S. Majumdar, D. Hanemann-Rawlings, E.M. Thomas, C. McGuiness, L. d'Alencon, M.L. Chabinyc, R.A. Segalman, Tailoring the Seebeck coefficient of PEDOT:PSS by controlling ion stoichiometry in ionic liquid additives, Chem. Mater. 30 (2018) 4816-4822.
[35] Z. Li, L. Deng, H. Lv, L. Liang, W. Deng, Y. Zhang, G. Chen, Mechanically robust and flexible films

of ionic liquid-modulated polymer thermoelectric composites, Adv. Funct. Mater. 31 (2021) 2104836.
[36] J. Luo, D. Billep, T. Waechtler, T. Otto, M. Toader, O. Gordan, E. Sheremet, J. Martin, M. Hietschold, D.R. Zahn, Enhancement of the thermoelectric properties of PEDOT:PSS thin films by post-treatment, J. Mater. Chem. A 1 (2013) 7576-7583.
[37] S.H. Lee, H. Park, W. Son, H.H. Choi, J.H. Kim, Novel solution-processable, dedoped semiconductors for application in thermoelectric devices, J. Mater. Chem. A 2 (2014) 13380-13387.
[38] M.H. Jeong, A. Sanger, S.B. Kang, Y.S. Jung, I.S. Oh, J.W. Yoo, G.H. Kim, K.J. Choi, Increasing the thermoelectric power factor of solvent-treated PEDOT:PSS thin films on PDMS by stretching, J. Mater. Chem. A 6 (2018) 15621-15629.
[39] C. Yi, A. Wilhite, L. Zhang, R. Hu, S.S. Chuang, J. Zheng, X. Gong, Enhanced thermoelectric properties of poly (3, 4-ethylenedioxythiophene):poly (styrenesulfonate) by binary secondary dopants, ACS Appl. Mater. Interfaces 7 (2015) 8984-8989.
[40] B. Zhang, J. Sun, H. Katz, F. Fang, R. Opila, Promising thermoelectric properties of commercial PEDOT:PSS materials and their Bi_2Te_3 powder composites, ACS Appl. Mater. Interfaces 2 (2010) 3170-3178.
[41] H. Ju, D. Park, K. Kim, J. Kim, Exfoliated Sn-Se-Te based nanosheets and their flexible thermoelectric composites with poly (3, 4-ethylenedioxythiophene):Poly (styrenesulfonate) fabricated by solution processing, Org. Electron. 71 (2019) 131-135.
[42] C. Yu, K. Choi, L. Yin, J.C. Grunlan, Light-weight flexible carbon nanotube based organic composites with large thermoelectric power factors, ACS nano 5 (2011) 7885-7892.
[43] M. Bharti, A. Singh, G. Saini, S. Saha, A. Bohra, Y. Kaneko, A. Debnath, K. Muthe, K. Marumoto, D. Aswal, Boosting thermoelectric power factor of free-standing Poly (3, 4ethylenedioxythiophene):polystyrenesulphonate films by incorporation of bismuth antimony telluride nanostructures, J. Power Sources 435 (2019) 226758.
[44] F. Jiang, J. Xiong, W. Zhou, C. Liu, L. Wang, F. Zhao, H. Liu, J. Xu, Use of organic solvent-assisted exfoliated MoS_2 for optimizing the thermoelectric performance of flexible PEDOT:PSS thin films, J. Mater. Chem. A 4 (2016) 5265-5273.
[45] N. Saxena, J. Keilhofer, A.K. Maurya, G. Fortunato, J. Overbeck, P. Müller-Buschbaum, Facile Optimization of thermoelectric properties in PEDOT:PSS thin films through acido-base and redox dedoping using readily available salts, ACS Appl. Energy Mater. 1 (2018) 336-342.
[46] Z. Fan, P. Li, D. Du, J. Ouyang, Significantly enhanced thermoelectric properties of PEDOT:PSS films through sequential post-treatments with common acids and bases, Adv. Energy Mater. 7 (2017) 1602116.
[47] C. Wang, K. Sun, J. Fu, R. Chen, M. Li, Z. Zang, X. Liu, B. Li, H. Gong, J. Ouyang, Enhancement of conductivity and thermoelectric property of PEDOT:PSS via acid doping and single post-treatment for flexible power generator, Adv. Sustainable Syst. 2 (2018) 1800085.
[48] S. Wei, L. Liu, X. Huang, Y. Zhang, F. Liu, L. Deng, E. Bilotti, G. Chen, Flexible and Foldable Films of SWCNT Thermoelectric Composites and an S-Shape Thermoelectric Generator with a Vertical Temperature Gradient, ACS Appl. Mater. Interfaces (2022).
[49] E. Dauzon, A.E. Mansour, M.R. Niazi, R. Munir, D.-M. Smilgies, X. Sallenave, C. Plesse, F. Goubard, A. Amassian, Conducting and stretchable PEDOT:PSS electrodes: Role of additives on self-assembly, morphology, and transport, ACS Appl. Mater. Interfaces 11 (2019) 17570-17582.
[50] C.M. Palumbiny, F. Liu, T.P. Russell, A. Hexemer, C. Wang, P. Müller-Buschbaum, The crystallization of PEDOT:PSS polymeric electrodes probed in situ during printing, Adv. Mater. 27 (2015) 3391-3397.
[51] P. Zhang, H.-y. Huang, Y. Chen, S. Yu, C. Krywka, S.K. Vayalil, S.V. Roth, T.-b. He, Preparation of long-range ordered nanostructures in semicrystalline diblock copolymer thin films using micromolding, Chin. J. Polym. Sci. 32 (2014) 1188-1198.
[52] P. Zhang, A. Rothkirch, M. Koch, S. Roth, T. Kraus, Determination of the surface facets of gold nanorods in wet-coated thin films with grazing‐incidence wide angle X-ray scattering, Part Part Syst Char 36 (2019) 1900323.
[53] P. Müller‐Buschbaum, The active layer morphology of organic solar cells probed with grazing incidence scattering techniques, Adv. Mater. 26 (2014) 7692-7709.
[54] H.G. Kim, B. Kang, H. Ko, J. Lee, J. Shin, K. Cho, Synthetic tailoring of solid-state order in diketopyrrolopyrrole-based copolymers via intramolecular noncovalent interactions, Chem. Mater. 27 (2015) 829-838.
[55] Y. Lu, Z.D. Yu, R.Z. Zhang, Z.F. Yao, H.Y. You, L. Jiang, H.I. Un, B.W. Dong, M. Xiong, J.Y. Wang, Rigid coplanar polymers for stable n-type polymer thermoelectrics, Angew. Chem. 131 (2019) 11512-

11516.
[56] X. Crispin, S. Marciniak, W. Osikowicz, G. Zotti, A.D. Van Der Gon, F. Louwet, M. Fahlman, L. Groenendaal, F. De Schryver, W.R. Salaneck, Conductivity, morphology, interfacial chemistry, and stability of poly (3, 4-ethylene dioxythiophene)-poly (styrene sulfonate): A photoelectron spectroscopy study, J. Polym. Sci., Part B: Polym. Phys. 41 (2003) 2561-2583.
[57] Z. Yu, Y. Xia, D. Du, J. Ouyang, PEDOT:PSS films with metallic conductivity through a treatment with common organic solutions of organic salts and their application as a transparent electrode of polymer solar cells, ACS Appl. Mater. Interfaces 8 (2016) 11629-11638.
[58] K. Sun, Y. Xia, J. Ouyang, Improvement in the photovoltaic efficiency of polymer solar cells by treating the poly (3, 4-ethylenedioxythiophene): poly (styrenesulfonate) buffer layer with co-solvents of hydrophilic organic solvents and hydrophobic 1, 2-dichlorobenzene, Sol Energ Mat Sol C 97 (2012) 89-96.
[59] B. Chu, B.S. Hsiao, Small-angle X-ray scattering of polymers, Chem. Rev. 101 (2001) 1727-1762.
[60] T. Li, A.J. Senesi, B. Lee, Small angle X-ray scattering for nanoparticle research, Chem. Rev. 116 (2016) 11128-11180.
[61] P. Zhang, R. Zou, S. Wu, L.-A. Meyer, J. Wang, T. Kraus, Gold nanoprobes exploring the ice structure in the aqueous dispersion of poly (ethylene glycol)-gold hybrid nanoparticles, Langmuir 38 (2022) 2460-2466.
[62] Y.Q. Zheng, Z.F. Yao, T. Lei, J.H. Dou, C.Y. Yang, L. Zou, X. Meng, W. Ma, J.Y. Wang, J. Pei, Unraveling the solution-state supramolecular structures of donor-acceptor polymers and their influence on solid-state morphology and charge-transport properties, Adv. Mater. 29 (2017) 1701072.
[63] L. Deng, X. Huang, H. Lv, Y. Zhang, G. Chen, Unravelling the mechanism of processing protocols induced microstructure evolution on polymer thermoelectric performance, Appl. Mater. Today 22 (2021) 100959.
[64] A. Hassan, L.J. Macedo, F.N. Crespilho, Recognizing conductive islands in polymeric redox surfaces using electrochemical-coupled vibrational spectromicroscopy, Chem. Commun. 56 (2020) 10309-10312.
[65] D.C. Martin, J. Wu, C.M. Shaw, Z. King, S.A. Spanninga, S. Richardson-Burns, J. Hendricks, J. Yang, The morphology of poly (3, 4-ethylenedioxythiophene), Polymer Reviews 50 (2010) 340-384.
[66] Q. Zhao, R. Jamal, L. Zhang, M. Wang, T. Abdiryim, The structure and properties of PEDOT synthesized by template-free solution method, Nanoscale Res. Lett. 9 (2014) 1-9.
[67] Y. Qin, Y. Xiao, L.-D. Zhao, Carrier mobility does matter for enhancing thermoelectric performance, APL Materials 8 (2020) 010901.
[68] S. Wei, Y. Zhang, H. Lv, L. Deng, G. Chen, SWCNT network evolution of PEDOT:PSS/SWCNT composites for thermoelectric application, Chem. Eng. J. 428 (2022) 131137.

Declaration of Competing Interest

The authors declare that they have no known competing financial interests or personal relationships that could have appeared to influence the work reported in this paper.